

Band Gap Narrowing and Electrical Properties of $(1-x)\text{BaTiO}_3\text{-}x\text{SrFe}_0.5\text{Nb}_0.5\text{O}_3$ Lead-Free Ceramics

Jianxin Chen

East China Normal University <https://orcid.org/0000-0002-6412-3814>

Hongmei Deng

Shanghai University

Dongliang Zheng

East China Normal University

Yanlin Pan

East China Normal University

Shufang Si

East China Normal University

Yuemin Zhang

East China Normal University

Pingxiong Yang (✉ pxyang@ee.ecnu.edu.cn)

East China Normal University

Junhao Chu

East China Normal University

Original Research

Keywords: Ceramics, Phase transformation, Optical behaviors, Ferroelectric properties

Posted Date: February 4th, 2021

DOI: <https://doi.org/10.21203/rs.3.rs-173217/v1>

License:  This work is licensed under a Creative Commons Attribution 4.0 International License.

[Read Full License](#)

Version of Record: A version of this preprint was published at Journal of Materials Science: Materials in Electronics on March 20th, 2021. See the published version at <https://doi.org/10.1007/s10854-021-05672-5>.

Abstract

The composite materials in the form of $(1-x)\text{BaTiO}_3-x\text{SrFe}_{0.5}\text{Nb}_{0.5}\text{O}_3((1-x)\text{BT}-x\text{SFN})$ are synthesized via the solid-state reaction route. Structure, optical behaviors and electrical properties of $(1-x)\text{BT}-x\text{SFN}$ are studied. It can be noted that the structure of the synthesized solid solution changes from the tetragonal phase to the cubic phase with increase of x -value. Due to the increase in content of double perovskite SFN, the optical band gaps of doped BT decrease to a minimum of 2.66 eV, which is smaller than that of pure BT (3.21 eV). However, the ferroelectric property deteriorates with the addition of dopants, which result from the lattice distortion caused by the substitution of Sr^{2+} and $\text{Fe}^{3+}/\text{Nb}^{5+}$ for Ba^{2+} and Ti^{4+} , respectively. These results provide new insights into the control of the structure, optical behaviors and ferroelectric properties in BT-based oxides.

1. Introduction

Ferroelectric materials are a type of multifunctional materials with built-in electric field of spontaneous polarization. Among these materials, especially perovskite materials with ABO_3 format, are of great concern because of their select electrical, mechanical, and thermal properties and can be prepared by a number of low-cost methods [1]. The ABO_3 -type materials possess an octahedral structure and the physical properties are controlled by A- and B-site cations. Conventional lead-containing perovskite materials, such as PTO and $\text{Pb}(\text{Mg}, \text{Nb}, \text{Yb}, \text{Ti})\text{O}_3$, have been commonly used in a variety of applications due to their fascinating electrical properties [2, 3]. However, the toxicity of lead oxide used in traditional based perovskite materials is not environmentally friendly, so it is essential to develop lead-free perovskite ceramics [4]. In the past few years, lead-free perovskite materials based on BaTiO_3 , KNbO_3 , and BiTiO_3 have achieved some progress [5–7], especially BaTiO_3 (BT) has been extensively devoted to some electronic devices [8–11], such as sensors and memory thanks to the excellent dielectric and ferroelectric properties, low toxicity and high chemical stability. BT exhibits different structural phases in different temperature ranges. That are, BT presents a tetragonal phase in the range of $278 \text{ K} < T < 393 \text{ K}$, a cubic phase at $393 \text{ K} < T < 1733 \text{ K}$, and a hexagonal phase for $T > 1733 \text{ K}$ [12]. Recently, many solid solutions based on BT or modified BT have been reported for their electrical properties. For example, $(\text{Ba}, \text{Ca})(\text{Sn}, \text{Ti})\text{O}_3$ ceramics presented excellent piezoelectric ($d_{33} = 630 \text{ pC/N}$) properties [13], and a high piezoelectric coefficient was showed in B_2O_3 -doped $\text{Ba}(\text{Zr}_{0.07}\text{Ti}_{0.93})\text{O}_3$ [14].

Double perovskite ($\text{A}_2\text{B}'\text{B}''\text{O}_6$), a special type of perovskite ABO_3 , has received more attention due to its rich properties such as multiferroic and high dielectric properties [15, 16]. In the double perovskites of $\text{A}_2\text{B}'\text{B}''\text{O}_6$ -type, A-site is generally the ions with large radius (Ba^{2+} , Sr^{2+} , Bi^{3+} , etc.), and B' / B'' -sites are generally the ions with small radius (Ti^{4+} , Fe^{3+} , Nb^{5+} , etc.) [17]. Compared with simple ABO_3 -type materials, the properties of $\text{A}(\text{B}'\text{B}'')\text{O}_3$ materials are dominated by the difference in charge and radius between cations at the B-site. $\text{SrFe}_{0.5}\text{Nb}_{0.5}\text{O}_3$ has been reported for fascinating dielectric property in many literatures [18, 19]. Sr^{2+} ions replace Ba^{2+} ions at the A-site in the BT-based system, which has attracted

wide attention due to its excellent response to the applied electric field. Based on this property, BST material has been used in a variety of electronic devices such as tunable capacitors and filters [20]. Moreover, the substitution of Ba^{2+} ions with Sr^{2+} ions can reduce the dielectric Curie temperature and greatly increase the dielectric constant [21]. Hansen et al. [22] reported that the substitution of Sr^{2+} ions for Ba^{2+} ions is conducive to obtaining better surface properties, maintaining the tetragonal lattice of BT, and thus improving its electrical performance. Therefore, based on these properties, double perovskite $\text{SrFe}_{0.5}\text{Nb}_{0.5}\text{O}_3$ is concerned.

In addition, one of the reasons that ferroelectric materials have attracted great attention is their potential applications in functional devices such as photovoltaic devices [1, 23, 24]. However, the wide band gap of ferroelectric materials is one of the main obstacles that seriously hinder them in photovoltaic applications. The band gap is generally above 3.0 eV, which means that ferroelectric materials have a wide absorption range in ultraviolet and little absorption in visible light. The conduction and valence band of ABO_3 perovskite ferroelectric are composed of d orbital of the transition metal ion and $\text{O-}2p$ orbital, respectively, and the band gap depends on the energy difference between their conduction band and valence band. In recent years, many studies have found that doping transition metal ions at the B-site (such as Fe^{3+} , Co^{2+} and Ni^{2+}) can effectively decrease the bandgap of materials, thus improving the absorption efficiency of light. According to Lou et al. [25], when Ni^{2+} and Nb^{5+} ions are added to pure BT, the band gaps decrease from 2.8eV of pure BT to 1.2eV of doped BTNN, which clearly indicates that the band gaps are significantly reduced by doping with Ni^{2+} ions, a transition metal. Yu et al. [26] doped $\text{BaFe}_{1/2}\text{Nb}_{1/2}\text{O}_3$ of double perovskite structure into KNbO_3 to reduce its band gap to 2.28eV, demonstrating that the doped materials have a larger visible light absorption range. Wang et al. also reported similar results of band gap reduction in doped $\text{Bi}_6\text{Fe}_2\text{Ti}_3\text{O}_{18}$ [27].

Up to now, there are few studies on doping SFN into BT, so the study on its performance is still worth further exploration. Here, we have synthesized $(1-x)\text{BT-xSFN}$ ceramics using a solid-state reaction route, and have explored structure, optical behaviors and ferroelectric properties of the ceramics. The present study provides an insight into the control of the performance of BT-based perovskite oxides.

2. Experimental Details

$(1-x)\text{BT-xSFN}$ polycrystalline ceramics with compositions $x = 0.00, 0.02, 0.05, 0.10, 0.15$ were prepared using a solid-state sintering process. The starting materials include BaCO_3 (99%), TiO_2 (99%), SrCO_3 (99%), Fe_2O_3 (99%) and Nb_2O_5 (99.99%). For each sample, initially, the raw powders were weighed in a stoichiometric ratio, mixed in the ethanol medium containing zirconia balls and ball-milled for 10 hours. Then the ball-milled mixtures were dried at 100 °C for 1 h and pre-sintered at 850 °C for 4 h. To obtain a better solid solution, the presintered powders were ground a second time for 8 h, then axial compressed to form cylindrical pellets (6 mm diameter and 2 mm thickness) with additive PVA binder (5 wt% polyvinyl alcohol) for more adequate reaction during calcination. Finally, the pellets were calcined to remove the

binder at 600 °C for 2 h, and then sintered at 1250 °C for 4 h. All materials were presintered and calcined in a covered alumina crucible with the heating and cooling rates of 5 °C/min and 4 °C/min respectively.

The structure and phase composition of all ceramics were investigated by X-ray diffraction (XRD) analysis and Raman spectroscopy. The XRD patterns were analyzed using Jade software and the crystal lattice parameters of the samples were provided. The microstructures of the samples were detected via a scanning electron microscopy (SEM). The optical absorption was observed via ultraviolet-visible-near-infrared (UV-vis-NIR) spectrophotometer. Polarization vs electric field (P - E) hysteresis loops were performed by a ferroelectric measuring system. Prior to the P - E test, the silver paste is applied to two surfaces of the polished pellets as two electrodes. After that, the ceramics were calcined to better attach the two electrodes to the surfaces of the pellets at 500 °C for 0.5 h.

3. Results And Discussion

The XRD patterns of the (1- x)BT- x SFN ($x = 0.00, 0.02, 0.05, 0.10, 0.15$) ceramics at 2θ of 10°-70° are depicted in Fig. 1(a), corresponding to a polycrystalline perovskite structure. Notice that no impurity peaks (such as Fe_2O_3 and Nb_2O_5) are observed. The peaks of the prepared pure BT are indexed as the tetragonal structure of the $P4mm$ space group (PDF#05-0626), which is consistent with the earlier report [28]. It is clearly observed from Fig. 1(b) that the diffraction peak (110) shifts toward higher angle with the addition of SFN at around 31.5° in XRD patterns, which confirms lattice distortion of the doped samples [29, 30]. The reduction of the lattice spacing (d) is calculated by the Bragg diffraction equation [31]: $2d\sin\theta = n\lambda$ (θ : the diffraction peak angle, λ : the wavelength of the X-ray). As illustrated in Fig. 1(c), the prepared pure BT has two diffraction peaks of (002) and (200) at around 45° in XRD. The intensity of peak (002) decrease for the $x = 0.02$ composition, and then (002) and (200) peaks gradually combine to form a single peak as the x above 0.02, which indicates a transformation of structure from tetragonal to cubic phase. Furthermore, in order to observe the structure more clearly, the lattice parameters of the as-synthesized samples are displayed in Fig. 2. On the whole, the lattice constant c tends to decrease with the x -value increasing, whereas the lattice constant a first increases until $x = 0.02$, and then becomes consistent with the lattice constant c as the x above 0.05. In addition, the decreased unit cell volumes are observed with the increase of SFN content in Fig. 2, which can be considered as the result of Ba^{2+} ($r = 1.35 \text{ \AA}$) being replaced by smaller Sr^{2+} ($r = 1.18 \text{ \AA}$). At the same time, the larger Fe^{3+} ($r = 0.65 \text{ \AA}$) and Nb^{5+} ($r = 0.64 \text{ \AA}$) substitute for Ti^{4+} ($r = 0.61 \text{ \AA}$) at the B-site, which is beneficial to reduce the excessive distortion of the lattice.

To further study the structural phase transformation of the synthesized solid solution, the RT Raman spectra of (1- x)BT- x SFN samples have been performed in the scope of 100–1000 cm^{-1} , as depicted in Fig. 3. All characteristic bands of pure BT are observed in the Raman spectrum. The vibration modes correspond to the $A_1(\text{TO}_1)$ at 262 cm^{-1} , the $E(\text{TO})$ at 305 cm^{-1} , the $A_1(\text{TO}_2)$ at 516 cm^{-1} , and the $A_1(\text{LO}_2)$ at 717 cm^{-1} , respectively, which can be provided by previous reports [32, 33]. Any transition of the broad peak at 262 cm^{-1} indicates the change in position and occupancy of Ti^{4+} . Obviously, the peaks move

gradually to lower frequencies and present a broadening with increasing SFN levels, which may be caused by the substitution of larger Fe^{3+} and Nb^{5+} ions for Ti^{4+} ions, resulting in the distortion of local structure at the B-site. The E(TO) mode observed at 305 cm^{-1} exhibits that intensity of its sharp peak is weakened. Since the sharp peak characterises the tetragonal phase [33], it is confirmed that the structure of the materials changes from tetragonal phase to cubic phase with increase of SFN content. This is corresponding to the result of XRD measured. Broad character of the $A_1(\text{TO}_2)$ and the $A_1(\text{LO}_2)$ modes named are slightly offset to lower and higher frequencies, respectively, which can be attributed to the vibration of the BO_6 octahedron. In addition, two new vibration modes 1 and 2 are observed at 185 cm^{-1} and 648 cm^{-1} . The appearance of mode 1 is considered to be associated with the vibration of A-O, indicating the presence of clusters rich in Ba^{2+} and/or Sr^{2+} in the lattice, which can be explained by earlier literature [34]. The presence of mode 2 may be caused by the FeO_6 and NbO_6 octahedral vibrations due to addition of SFN doping, in which $\text{Fe}^{3+}/\text{Nb}^{5+}$ replace Ti^{4+} at the B-site. Similar results have also been reported earlier [35, 36].

The surface morphology of the prepared ceramics at 1250°C is characterized by SEM, as presented in Fig. 4(a)-(e). The microstructure of pure BT ceramics displays clearly visible particles and no evident agglomeration of grains, which suggests that the pure BT prepared has favorable crystallization. However, with the increase of doping content, some pores appear among the grains, and the grains are obviously agglomerated. Further, compared with pure BT, the grain size exhibit uneven distribution for $x = 0.02$, that is, the large and small grains are close to each other, and a trend that the grain size decreases can be detected from the SEM images. However, for the x above 0.02, the grain size distribution is relatively uniform, and the grain size is outstanding different from that of the group divided into 0.00 and 0.02. As a whole, the grain size of SFN-doped BT has been significantly reduced, which reflects that the addition of the dopant restrains the growth of the grains. This may be caused by some stresses during calcination by solid solution reaction, which hinders the movement of the grain boundary and thus reduces the grain size [37, 38]. It is also possible that due to the incorporation of SFN, the mismatch between Fe, Nb and Ti with different ion radii at the B-site leads to the increase of lattice distortion, thus inhibiting the growth of grains [39, 40].

Figure 5(a) depicts the optical absorption spectra of the synthesized materials measured by UV-vis-NIR spectrophotometer. The absorption edge is about 400 nm for pure BT, while the absorption edge gradually widths and transfers to higher wavelength with the increase of doping for doped BT, suggesting that doped BT samples possess greater light absorption scope. It is well known that the variation of the absorption edge in the absorption spectrum is strongly related to the optical band gap (E_g) of the materials. In order to obtain E_g of $(1-x)\text{BT}-x\text{SFN}$, the light absorption spectra are derived by the Kubelka-Munk function [19, 41]: $F(R) = (1-R)^2/(2R) = \alpha/s$ (R : the relative reflectivity of the materials; α : absorbance; s : scattering coefficient). The E_g are obtained by the tangent line of the Tauc plot, where the expression of Tauc plot is $(ah\nu)^n = C(h\nu - E_g)$ (h : Planck's constant; ν : frequency; C : proportional constant; n : 2 and 1/2, corresponding direct and indirect band gaps, respectively) [42, 43]. Thus, for materials synthesized on the

basis of BT with a direct bandgap, the value of n is 2. Figure 5(b) display the Tauc plots of $(1-x)\text{BT}-x\text{SFN}$ materials. Through the intersection point of Tauc tangent and the horizontal axis, it can be clearly observed that the E_g of pure BT is 3.21 eV, which is consistent with earlier reports [44, 45]. The E_g of the doped BT ($x = 0.02, 0.05, 0.10$ and 0.15) are 3.15, 3.04, 2.95 and 2.66 eV, respectively. This reveals E_g of $(1-x)\text{BT}-x\text{SFN}$ significantly lower with the increase of x , but not linearly. It can be divided into three parts: (i) $0 \leq x < 0.05$ ($\Delta E_g / \Delta x = 3.4$). (ii) $0.05 \leq x < 0.10$ ($\Delta E_g / \Delta x = 1.8$). (iii) $0.10 \leq x \leq 0.15$ ($\Delta E_g / \Delta x = 5.8$), as illustrated in Fig. 5(c).

The above optical behaviors can be interpreted via the doping mediation mechanism. Many reports have proved that in pure BT, the conduction band and valence band are chiefly constituted by Ti-3d orbital and O-2p orbital, respectively. The conduction band and valence band are primarily formed from Fe-3d orbital and O-2p orbital respectively for the pure SFN, which is similar to the orbital arrangement of $\text{BaFe}_{0.5}\text{Nb}_{0.5}\text{O}_3$ (BFNO) [46]. According to the relationship between the electronegativity of ions and the conduction band, the larger the electronegativity of ions, the lower the conduction band in terms of energy. In $(1-x)\text{BT}-x\text{SFN}$ ceramics, since the electronegativity of the Fe^{3+} ion is larger than that of the Ti^{4+} ion, in terms of energy, the Fe-3d orbital is lower than Ti-3d orbital, which makes the conduction band of doped BT materials transfer into the band gap, leading to the narrowing of the band gap. Furthermore, the incorporation of SFN into BT can also be considered to the introduction of $\text{Fe}^{3+}/\text{Nb}^{5+}$ ions at the B-site and Sr^{2+} at the A-site into pure BT. However, the substitution of Ti^{4+} with Fe^{3+} and Nb^{5+} ions of different radius will introduce O vacancy defects and distort the crystal lattice. This directly changes the energy band structure of BT, introducing defects in the band gap, which may be the reason why the edge of the energy band moves into the bandgap. The changes of energy band described above are shown in Fig. 5(d). The results indicate that the E_g of BT can be adjusted in a small range by controlling the optimized doping amount of SFN and the absorption properties can be improved in the visible range.

To better understand the ferroelectric properties of $(1-x)\text{BT}-x\text{SFN}$ with ions co-doping at the Ti-site, Fig. 6(a)-(e) present the RT polarization-electric field (P - E) hysteresis loops of all ceramics at frequency 1 kHz, where the applied electric field of the hysteresis loops of each sample corresponds to 10, 15 and 20 kV/cm, respectively. It is clearly observed that, for each sample, when the electric field changes from 10 to 20 kV/cm, the bigger and more saturated P - E hysteresis loops appear. The above phenomena may be caused by the enhancing of the stability of the ordered ferroelectric domains as the electric field increases [39]. For pure BT, roughly the standard hysteresis loops can be observed, which demonstrate the ferroelectric properties of ceramics [47, 48]. However, it is obvious that the hysteresis loops tend to be flatter and slimmer with the addition of higher doping. In the doped BT, when $x = 0.05$, the value of remnant polarization (P_r) is higher than that of $x = 0.02, 0.10$ and 0.15 , indicating that the doped BT at this concentration has better ferroelectric properties. With the addition of SFN, the weakening of ferroelectric polarization is noticed, which may be due to the substitution of Fe^{3+} ions for Ti^{4+} ions at the B-site, introducing more oxygen vacancy defects and thus hindering the movement of ferroelectric domains, resulting in the decrease of P_r [49]. As can be seen from Fig. 6, there is a large opening, which may be due to the leakage current caused by O vacancies introduced into the samples during the

calcination process. Therefore, from the analysis results, it is believed that enhancing the quality of as-prepared ceramics can reduce leakage current, thus improving the ferroelectric properties of the prepared samples.

4. Conclusions

In summary, the structure, optical behaviors and ferroelectric properties of (1-x)BT-xSFN solid solution prepared via solid reaction have been explored. XRD results show that with SFN concentration increasing, the structure of the synthesized samples changes from the tetragonal phase to the cubic phase. Raman analysis results display that the characteristic peak of the tetragonal phase gradually weakens with the increase of doping content, which further confirms the phase transition of the samples. The SEM micrograph reveals that the grain size of doped samples reduces significantly and the pores between the grains increase with higher doping. The optical absorption spectra illustrate that the E_g of (1-x)BT-xSFN decrease from 3.21 eV for pure BT to 2.66 eV for doped BT. The electric hysteresis loops suggest that the ferroelectric property tends to deteriorate with the addition of SFN. These results contribute to a better understanding of the properties of doped BT oxides.

Declarations

Acknowledgements

This work was supported by the National Natural Science Foundation of China (No. 61474045).

References

1. M. Qin, K. Yao, Y. C. Liang, Appl. Phys. Lett. **93**, 16 (2008).
2. Dahl, J. K. Grepstad, T. Tybell, J. Appl. Phys. **103**, 114112 (2008).
3. C. Duran, S. Dursun, E. Akça, Scr. Mater. **113**, 14 (2016).
4. R. Prangé, L. Pallier, K. C. Hansen, R. Howard, A. Vourlidis, R. Courtin, C. Parkinson, Nature. **432**, 78 (2004).
5. P. Redhu, R. Punia, A. Hooda, B. P. Malik, G. Sharma, P. Sharma, Ceram. Int. **46**, 17495 (2020).
6. I. Grinberg, D. V. West, M. Torres, G. Gou, D. M. Stein, L. Wu, G. Chen, E. M. Gallo, A. R. Akbashev, P. K. Davies, J. E. Spanier, A. M. Rappe, Nature. **503**, 509 (2013).
7. C. Xu, D. Lin, K. W. Kwok, Solid State Sci. **10**, 934 (2008).
8. C. Xu, R. Su, Z. Wang, Y. Wang, D. Zhang, J. Wang, J. Bian, C. Wu, X. Lou, Y. Yang, J. Alloys Compd. **784**, 173 (2019).
9. N. Raengthon, V. J. Derosé, G. L. Brennecka, D. P. Cann, Appl. Phys. Lett. **101**, 112904 (2012).
10. L. Zhang, W. Liu, W. Chen, X. Ren, J. Sun, E. A. Gurdal, S. O. Ural, K. Uchino, Appl. Phys. Lett. **101**, 242903 (2012).

11. P. Zheng, J. L. Zhang, S. F. Shao, Y. Q. Tan, C. L. Wang, *Appl. Phys. Lett.* **94**, 92 (2009).
12. P. P. Khirade, S. D. Birajdar, A. V. Raut, K. M. Jadhav, *Ceram. Int.* **42**, 12441 (2016).
13. L. F. Zhu, B. P. Zhang, L. Zhao, S. Li, Y. Zhou, X. C. Shi, N. Wang, *J. Eur. Ceram. Soc.* **36**, 1017 (2016).
14. P. Jarupoom, G. Rujijanagul, *J. Appl. Phys.* **114**, 1 (2013).
15. A. Rathi, H. Borkar, P. K. Rout, A. Gupta, H. K. Singh, A. Kumar, B. Gahtori, R. P. Pant, G. A. Basheed, *J. Phys. D. Appl. Phys.* **50**, 465001 (2017).
16. D. Choudhury, P. Mandal, R. Mathieu, A. Hazarika, S. Rajan, A. Sundaresan, U. V. Waghmare, R. Knut, O. Karis, P. Nordblad, D. D. Sarma, *Phys. Rev. Lett.* **108**, 1 (2012).
17. Z. Chu, H. Shi, W. Shi, G. Liu, J. Wu, J. Yang, S. Dong, *Adv. Mater.* **29**, 1 (2017).
18. Y. Y. Liu, X. M. Chen, X. Q. Liu, L. Li, *Appl. Phys. Lett.* **90**, 1 (2007).
19. N. Raengthon, T. Sebastian, D. Cumming, I. M. Reaney, D. P. Cann, *J. Am. Ceram. Soc.* **95**, 3554 (2012).
20. S. Suasmoro, S. Pratapa, D. Hartanto, D. Setyoko, U. M. Dani, *J. Eur. Ceram. Soc.* **20**, 309 (2000).
21. A. Jain, A. K. Panwar, R. Saroha, A. K. Jha, *J. Am. Ceram. Soc.* **100**, 5239 (2017).
22. P. Hansen, D. Hennings, H. Schreinemacher, *J. Electroceramics.* **2**, 85 (1998).
23. D. Cao, C. Wang, F. Zheng, W. Dong, L. Fang, M. Shen, *Nano Lett.* **12**, 2803 (2012).
24. Z. Gao, L. Liu, X. Han, X. Meng, L. Cao, G. Ma, Y. Liu, J. Yang, Q. Xie, H. He, *J. Am. Ceram. Soc.* **98**, 3930 (2015).
25. Q. Lou, J. Zeng, Z. Man, L. Zheng, C. Park, A. Kassiba, Y. Liu, X. Chen, G. Li, *J. Am. Ceram. Soc.* **102**, 7405 (2019).
26. L. Yu, H. Deng, W. Zhou, P. Yang, J. Chu, *Mater. Lett.* **202**, 39 (2017).
27. T. Wang, H. Deng, X. Meng, H. Cao, W. Zhou, P. Shen, Y. Zhang, P. Yang, J. Chu, *Ceram. Int.* **43**, 8792 (2017).
28. C. Srilakshmi, R. Saraf, V. Prashanth, G. M. Rao, C. Shivakumara, *Inorg. Chem.* **55**, 4795 (2016).
29. Z. Wen, G. Hu, S. Fan, C. Yang, W. Wu, Y. Zhou, X. Chen, S. Cui, *Thin Solid Films.* **517**, 4497 (2009).
30. N. Ding, H. Deng, P. Yang, J. Chu, *Mater. Lett.* **82**, 71 (2012).
31. J. J. Gu, G. L. Zhao, F. W. Cheng, J. R. Han, L. H. Liu, H. Y. Sun, *Phys. B Condens. Matter* **406**, 4400 (2011).
32. Y. Yang, Y. Zhou, J. Ren, Q. Zheng, K. H. Lam, D. Lin, *J. Am. Ceram. Soc.* **101**, 2594 (2018).
33. J. Pokorný, U. M. Pasha, L. Ben, O. P. Thakur, D. C. Sinclair, I. M. Reaney, *J. Appl. Phys.* **109**, 114110 (2011).
34. G. Schileo, L. Luisman, A. Feteira, M. Deluca, K. Reichmann, *J. Eur. Ceram. Soc.* **33**, 1457 (2013).
35. T. L. Phan, P. Zhang, D. Grinting, S. C. Yu, N. X. Nghia, N. V. Dang, V. D. Lam, *J. Appl. Phys.* **112**, 013909 (2012).
36. N. V. Dang, T. L. Phan, T. D. Thanh, V. D. Lam, L. V. Hong, *J. Appl. Phys.* **111**, 113913 (2012).
37. J. C. Shaw, K. S. Liu, I. N. Lin, *J. Mater. Sci.* **28**, 5534 (1993).

38. W. Zhou, H. Deng, L. Yu, P. Yang, J. Chu, J. Appl. Phys. **117**, 1 (2015).
39. P. Sharma, N. Berwal, N. Ahlawat, A. S. Maan, R. Punia, Ceram. Int. **45**, 20368 (2019).
40. B. Asbani, Y. Gagou, M. Trček, J. L. Dellis, M. Amjoud, A. Lahmar, D. Mezzane, Z. Kutnjak, M. El Marssi, J. Alloys Compd. **730**, 501 (2018).
41. S. K. Kar, S. Swain, Sonia, P. Kumar, Mater. Chem. Phys. **155**, 171 (2015).
42. J. Yu, Q. Xiang, M. Zhou, Appl. Catal. B Environ. **90**, 595 (2009).
43. G. Zhang, H. Wu, G. Li, Q. Huang, C. Yang, F. Huang, F. Liao, J. Lin, Sci. Rep. **3**, 1 (2013).
44. F. Yang, L. Yang, C. Ai, P. Xie, S. Lin, C. Z. Wang, X. Lu, Nanomaterials. **8**, 455 (2018).
45. S. Ramakanth, K. C. James Raju, J. Appl. Phys. **115**, 173507 (2014).
46. G. Zhang, S. Sun, W. Jiang, X. Miao, Z. Zhao, X. Zhang, D. Qu, D. Zhang, D. Li, Z. Sun, Adv. Energy Mater. **7**, 1600932 (2017).
47. J. A. Astudillo, S. A. Dionizio, J. L. Izquierdo, O. Morán, J. Heiras, G. Bolaños, AIP Adv. **8**, 1 (2018).
48. X. Mao, H. Sun, W. Wang, Y. Lu, X. Chen, Solid State Commun. **152**, 483 (2012).
49. J. F. Scott, C. A. Paz De Araujo, Science. **246**, 1400 (1989).

Figures

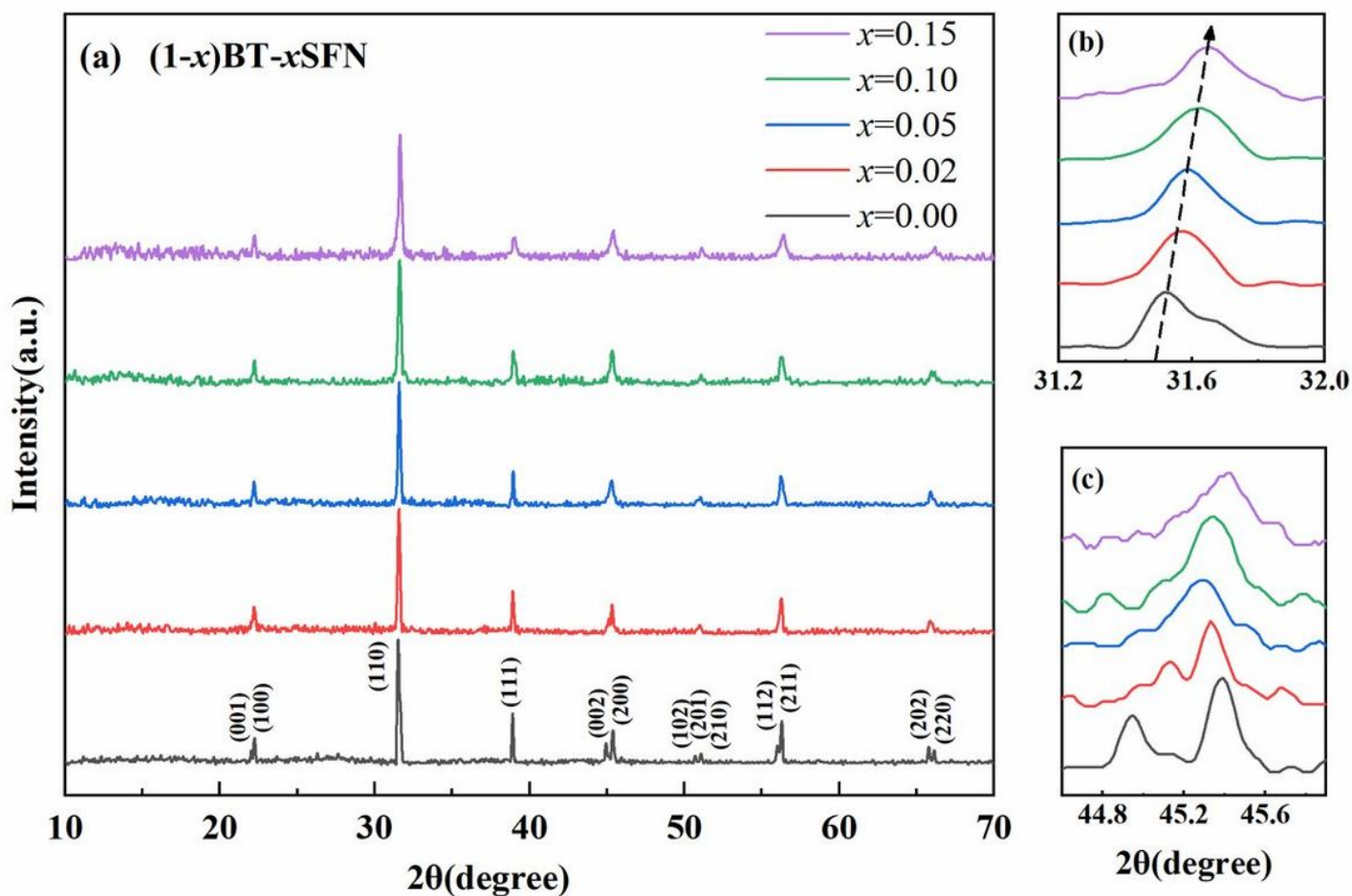


Figure 1

a XRD patterns of (1-x)BT-xSFN ceramics. b and c Enlarged patterns at $2\theta \sim 31.5^\circ$ and $\sim 45^\circ$, respectively

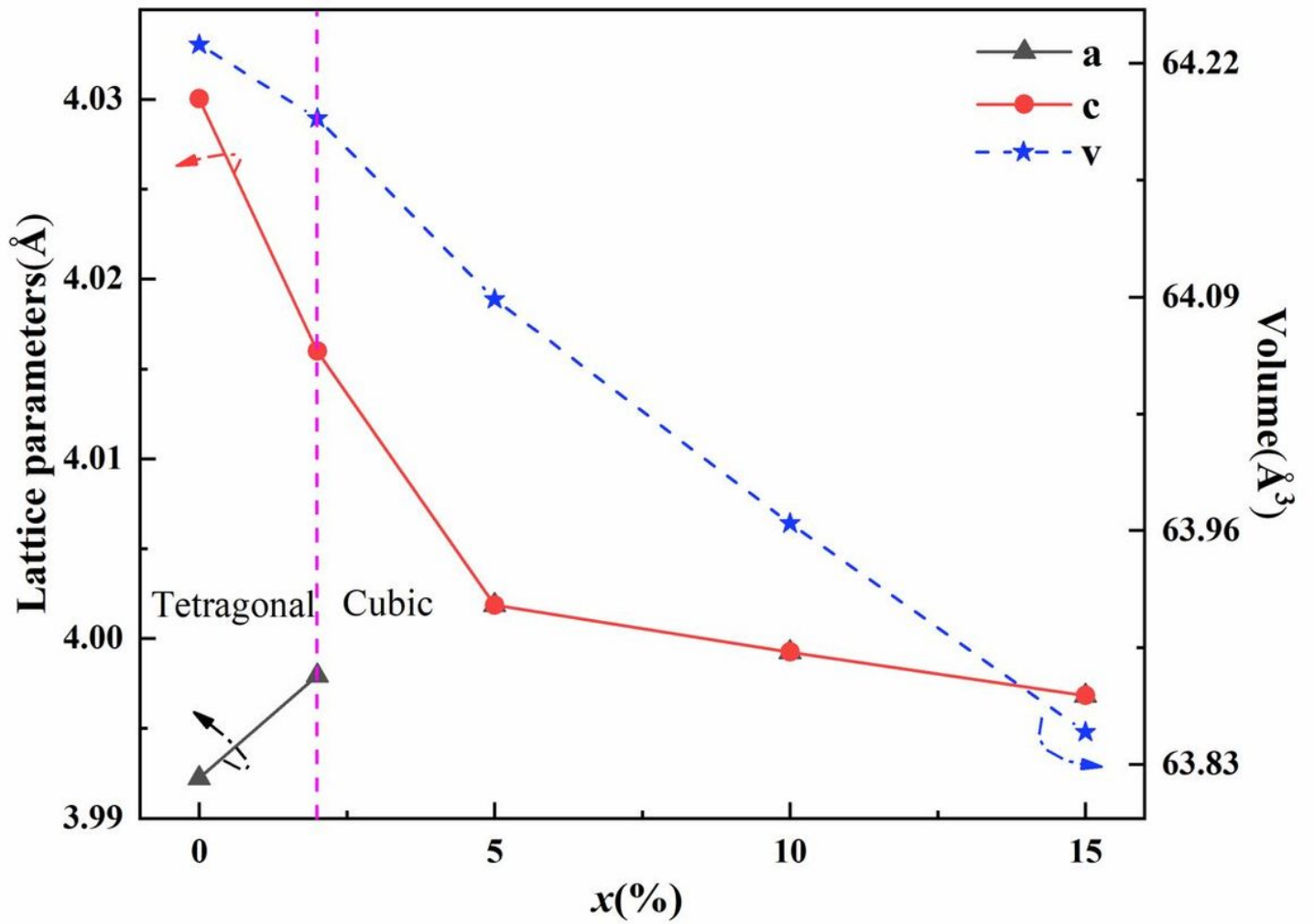


Figure 2

Lattice parameters and unit cell volume of (1-x)BT-xSFN versus x

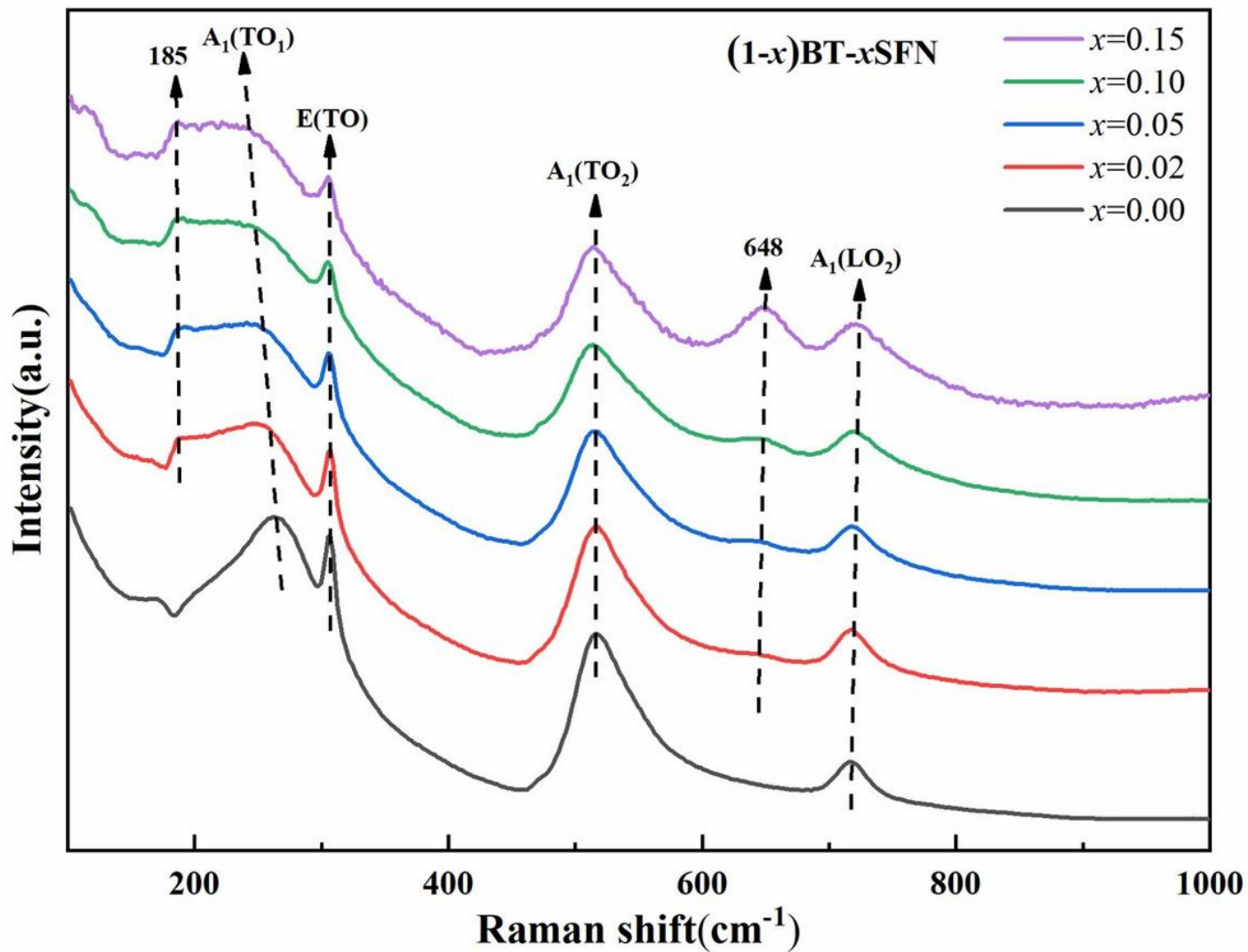


Figure 3

Raman spectra of $(1-x)\text{BT}-x\text{SFN}$ ceramics

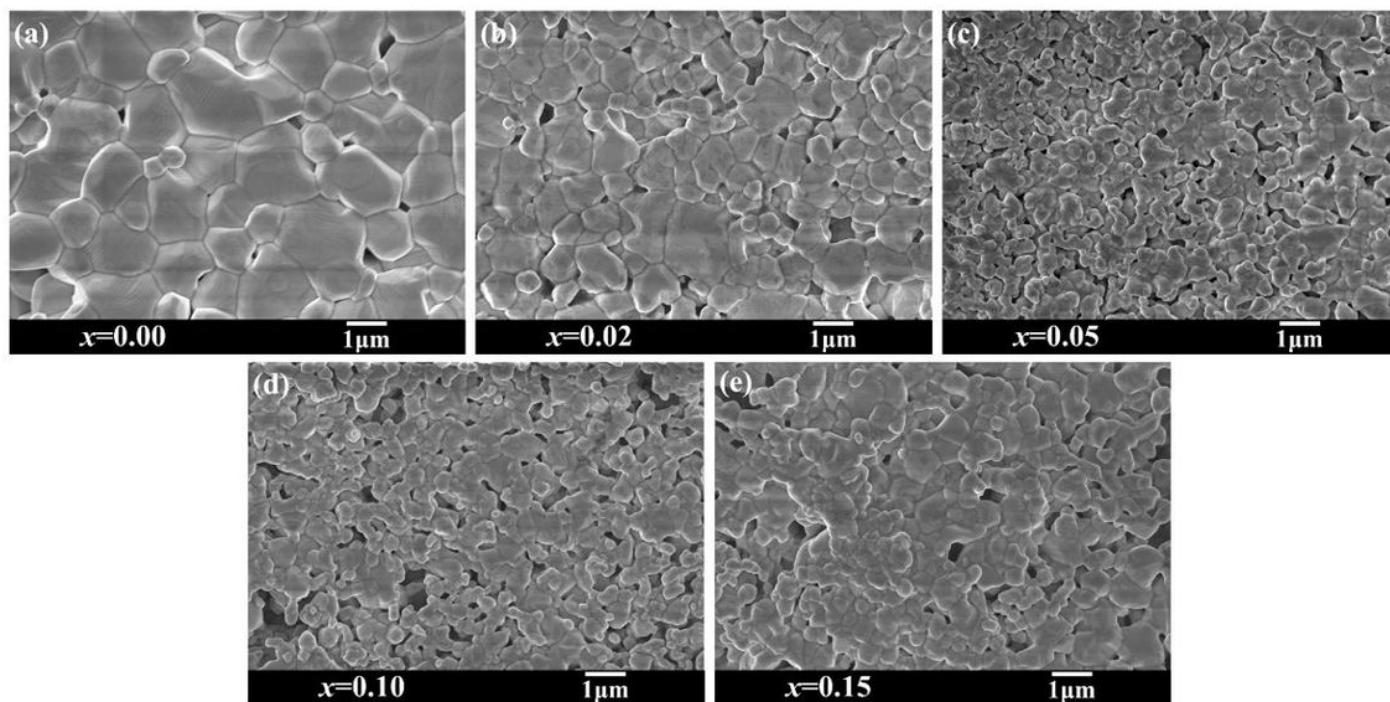


Figure 4

a-e SEM images of samples

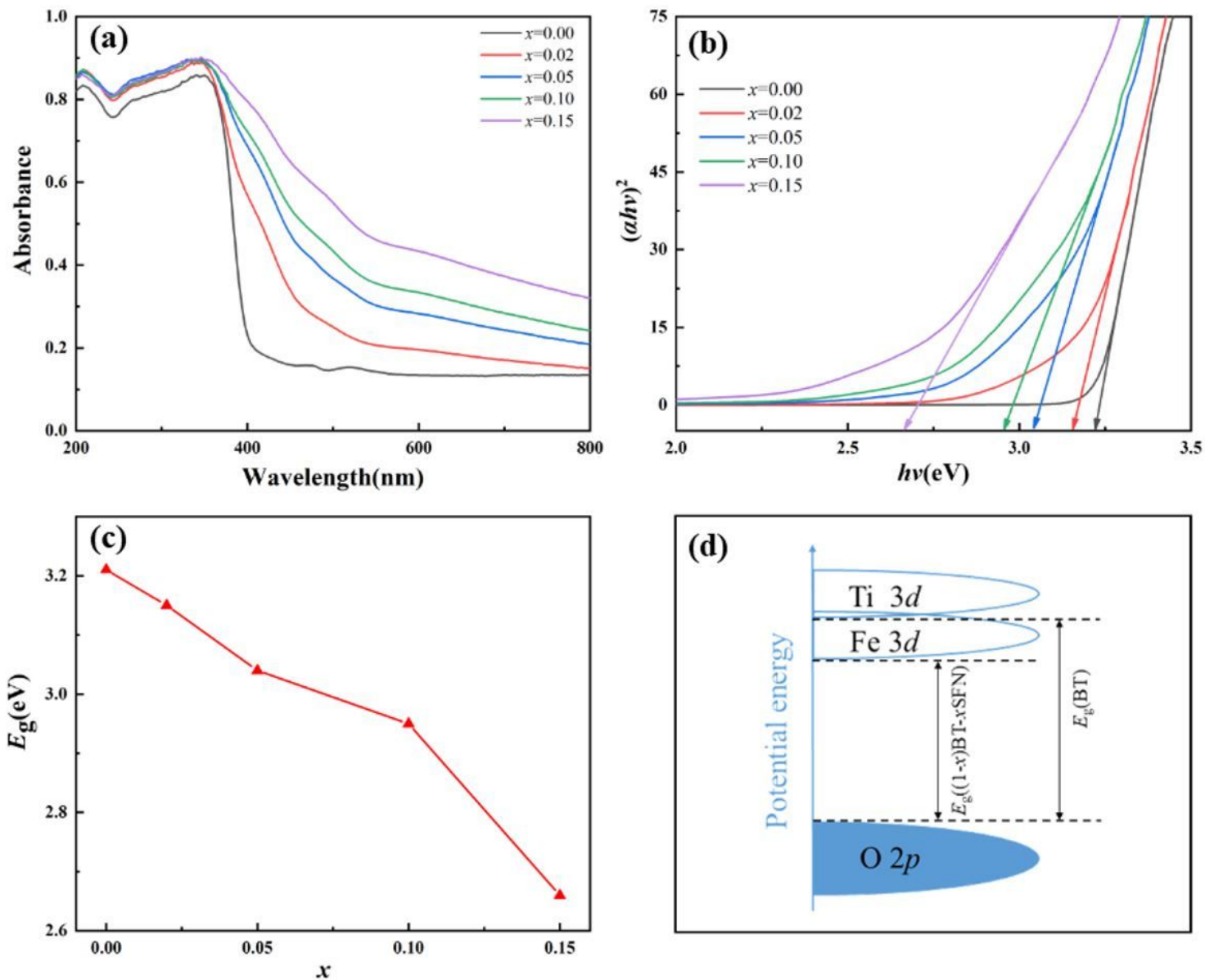


Figure 5

a UV-vis-NIR absorption spectra of the as-prepared samples. b Plots of $(ahv)^2$ vs $h\nu$ for the absorption spectra. c Variation of E_g for all samples. d A schematic diagram for the decrease of E_g

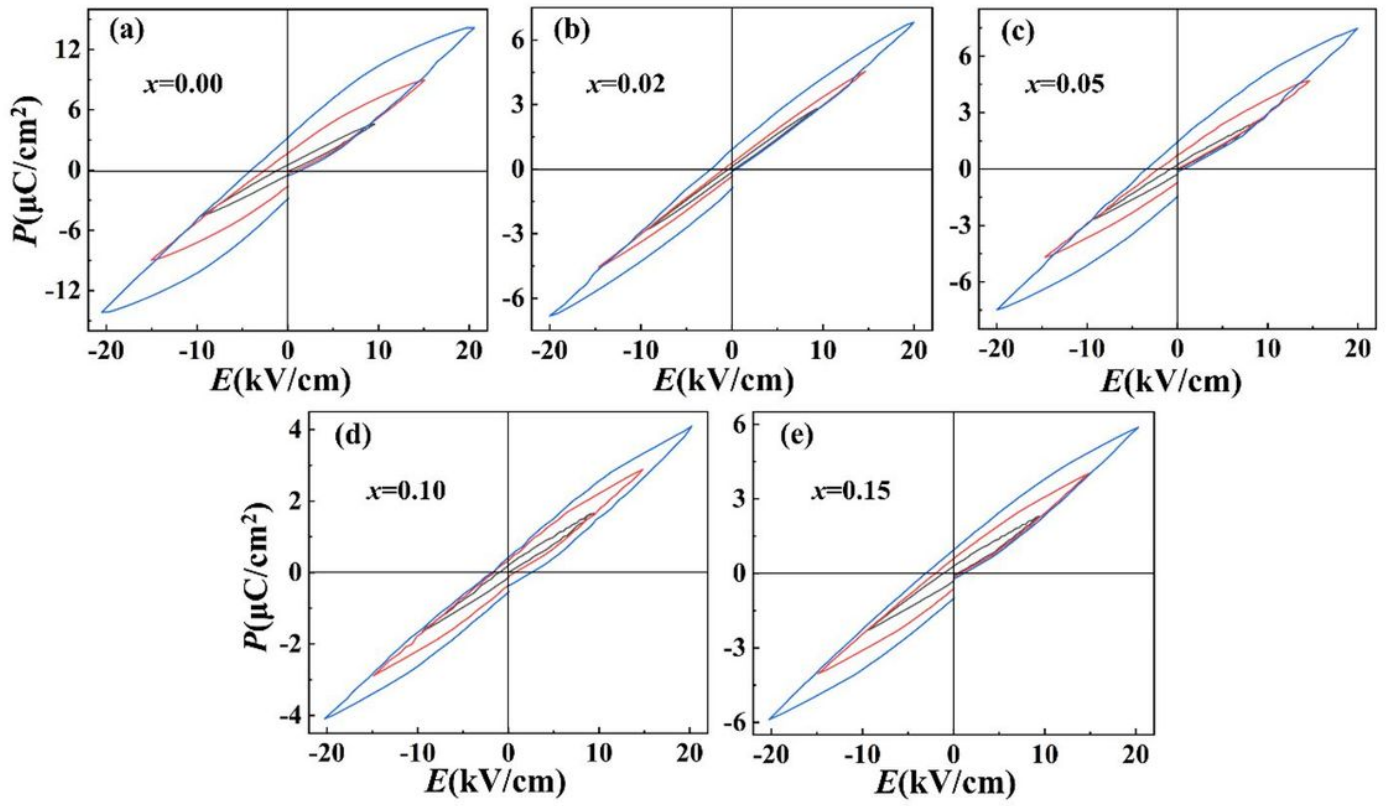


Figure 6

P-E curves of samples